# Anion (Fluoride)-Doped Ceria Nanocrystals: Synthesis, Characterization, and Its Catalytic Application to Oxidative Coupling of Benzylamines

Shahzad Ahmad, Kovuru Gopalaiah,* Sankala Naga Chandrudu, and Rajamani Nagarajan*

Department of Chemistry, University of Delhi, Delhi 110007, India

Ⓢ Supporting Information

ABSTRACT: Fluoride doping in the CeO_2 lattice has been achieved by a simple, reliable, reproducible, and safe solution-based method. F-containing CeO_2 has retained the fluorite structure, and its effect has been confirmed from various analytical techniques such as powder X-ray diffraction, Fourier transform IR, Raman, UV−visible diffuse reflectance, photoluminescence (PL), and X-ray photoelectron spectroscopy (XPS), scanning electron microscopy−energy-dispersive X-ray (EDX) and transmission electron microscopy−EDX analysis. The concentration of fluoride in the CeO_2 lattice has been determined from chemical analysis and core-level XPS analysis. The concentration of Ce^{3+} in the F-doped and undoped CeO_2 samples have been determined both from XPS analysis as well as from variable-temperature magnetic susceptibility measurements. The characteristic Ce^{3+} emission in the PL spectrum indicated the increase of Ce^{3+} ion concentration in the F-doped sample, conforming to the results from XPS and magnetic measurements. F-doped CeO_2 nanocrystals showed moderate monodispersity as determined from particle-size measurements using dynamic light scattering experiments and high surface area of 106.1 m^2/g. Optical band gap of CeO_2 has narrowed upon doping with fluoride ions from 3.05 to 2.95 eV. The formation of extrinsic oxygen vacancy complexes upon F-doping has been observed in the Raman spectrum (at 1097 cm^{-1}) in addition to fingerprint bands of CeO_2. The UV-shielding property and photocatalytic inactivity toward aqueous dye degradation process of F-doped CeO_2 has suggested its potential use in cosmetic applications. Both F-doped CeO_2 and CeO_2 have been used as catalysts for oxidative coupling of benzylamines to imines in the presence of molecular oxygen under solvent-free conditions. F-doped CeO_2 exhibited better catalytic efficiency than CeO_2. The oxidation procedure using these catalysts is simple, environmentally benign, and solvent-free, and the catalysts are reusable.
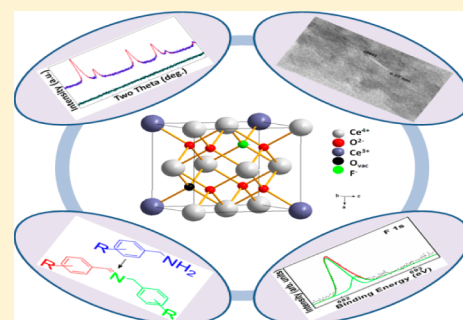
1. INTRODUCTION

Owing to the rich chemistry arising from the anion non-stoichiometry, research on various aspects of cerium oxide (CeO_2), including their applications as oxidation catalysts in automotives, gas sensors, and fuel and solar cells, has been on the rise.[1] While the inherent chemical properties of CeO_2, such as high oxygen storage capacity and oxygen mobility, depend on the Ce^{3+}/Ce^{4+} redox cycle, the function of CeO_2 as catalyst can be greatly influenced by its size, shape, and surface area. To widen the use of CeO_2, a variety of cations have been doped in the CeO_2 lattice. The rare earth- or transition metal-doped CeO_2 has found applications as catalysts in water gas shift reactions and CO oxidation.[2] Hegde et al.[3] have demonstrated the doping of Fe^{3+} in CeO_2 can increase the oxygen storage capacity of CeO_2. They have also established some efficient catalytic methods for NO reduction and hydrocarbon and CO oxidation by CeO_2 doped with noble metals (Pt, Pd, and Rh).[4] Taking advantage of its low refractive index (2.2), transparency to visible light, excellent UV shielding property, and natural appearance on the skin, silica- and ZnO-supported cation (Ca^{2+}, Fe^{2+})-doped and cation−anion (Ca^{2+}, F^-)-codoped CeO_2 systems have been suggested for use in personal-care products.[5]

While there are a number of studies on the effect of cation doping on the structure and properties,[6] limited reports are available on the singly anion-doped CeO_2.[7] The lack of a reliable method to incorporate the desired concentration of anion into the CeO_2 lattice is the major difficulty, as evidenced by the difference in the concentration of anion incorporated in the CeO_2 lattice. Solid−gas (ceria−NH_3) reactions, the sol−gel method followed by treatment with flowing ammonia gas, and a solution-based method employing ethylenediamine as the nitrogen source followed by controlled sintering have been reported in the literature for the synthesis of nitrogen-doped ceria.[7] As CeO_2 possesses a fluorite (CaF_2) structure, it is expected to accommodate fluoride ions in place of oxide ions in terms of structure. Jorda et al.[8] initially reported the inclusion of 7% fluoride ion in cubic CeO_2 from $CeO_{1.5}$−CeO_2−CeF_3 phase diagram studies in argon atmosphere, in which the effect of fluoride ion doping on the properties of CeO_2 have not been discussed. Demourgues and co-workers[5a] increased the concentration of fluoride ions in CeO_2 through the coupled substitution approach of Ca^{2+} for Ce^{4+} and F^- for O^{2-}. The

effects of single cationic substitution (Ca^{2+}) as well as the coupled substitution (Ca^{2+} and F^-) on the structure and properties of CeO_2 has been dealt with in detail by them.[5a] Notably, by both of the substitution approaches, the emergence of interesting UV-shielding properties of CeO_2 has been established and interpreted based on the change in the electropositive character of Ce^{4+} during these processes.[5a]

Interestingly, cerium prefers to exist in +4 oxidation state with oxide, but it forms CeF_3 (+3) with highly electronegative fluoride ions. Therefore, CeO_2 is the ideal candidate to incorporate fluoride ions, as the introduction of heterovalent anion can possibly result in the corresponding reduction of Ce^{4+} to Ce^{3+}, thus favoring increased concentration of a Ce^{3+}/Ce^{4+} redox couple. Furthermore, the inclusion of a heterovalent anion is expected to introduce changes in the electronic structure, potentially resulting in unusual properties, including the UV-shielding property. Given these facts, striving for the synthesis of fluoride-doped CeO_2 lattice meets with mammoth challenges. First, the gas–solid reactions of CeO_2 require the handling of hazardous fluoride sources such as HF, and an intricate setup is involved to handle F_2. Second, the slow kinetics (usually associated with the gas–solid reactions) may involve long hours of reactions and may lead to heterogeneous distribution of dopants in the samples. Finally, the enormous driving force to precipitate the insoluble CeF_3 under aqueous conditions may hamper the effective fabrication of uniformly F-doped crystalline CeO_2. Our strategy to dope fluoride ion in the CeO_2 lattice was to use tetrabutylammonium fluoride (1.0 M in tetrahydrofuran (THF)) as the fluorinating agent and ethylenediamine as the base with which the pH of the cerium(III) nitrate solution was varied at room temperature. The obtained phase was thoroughly analyzed by a variety of diffraction, microscopy, and spectroscopy techniques.

Ceria and cation-doped ceria have been employed as heterogeneous catalysts for many organic transformations such as allylic oxidations, hydrogenation of nitroarenes, oxidation of alcohols, and transalkylation reactions.[9] Nitrogen-doped ceria has been investigated primarily as a photocatalyst for the degradation of harmful organics, including acetaldehyde.[7d] The oxidation of amines to imines is of current and intense interest, owing to the importance of imines as versatile synthetic intermediates. In particular, imines can act as electrophilic reagents in many transformations such as alkylations, condensations, and cycloadditions, including aza-Diels–Alder reactions.[10] Imines also serve as starting materials for the synthesis and racemisation of chiral amines, which are important intermediates in the preparation of biologically active compounds.[11] While a number of procedures have been developed for the oxidation of amines to imines, a persistent challenge is the control of reaction pathways to avoid undesired byproducts such as nitriles and aldehydes. For selective oxidation of primary amines to imines, notable examples of procedures based on transition-metal catalysts include copper,[12] gold,[13] iron,[14] platinum,[15] vanadium[16] complexes, and photoinduced aerobic oxidation by TiO_2[17] and Nb_2O_5.[18] Despite their applicability, many of these methods suffer from the requirement of large quantities of additives such as oxidants and electron-transfer mediators. Furthermore, the use of unfriendly organic solvents in these reactions is a greater concern. From the practical point of view, these procedures may cause severe deactivation of the catalysts and/or the formation of significant amounts of byproducts. Recently, Jones and co-workers[19] explored CuO, CeO_2, and CuO-supported CeO_2 catalysts in

the aerobic oxidative homocoupling of benzylamine to form *N*-benzylidenebenzylamine in dimethyl sulfoxide (DMSO). Herein we report the synthesis, characterization, and application of F-doped CeO_2 as catalyst for the oxidative coupling of benzylamines to imines in the presence of molecular oxygen under solvent-free conditions. Under similar conditions, undoped CeO_2 has also been evaluated for its catalytic function.

2. EXPERIMENTAL SECTION

2.1. Synthesis of F-Doped CeO_2 and CeO_2. In a 250 mL round-bottomed flask, $Ce(NO_3)_3 \cdot 6H_2O$ (4.36 g, 10 mmol) was dissolved in 50 mL of double-distilled water. To this solution, ethylenediamine was added dropwise until the pH increased to 9.8. The resulting mixture was stirred overnight, with pH maintained at 9.8. The yellow suspension obtained was centrifuged and washed several times with water. For the synthesis of 10 mol % F-doped CeO_2, the aqueous solution of $Ce(NO_3)_3 \cdot 6H_2O$ (3.924 g, 9 mmol) was added to a mixture containing tetrabutylammonium fluoride (1.0 M in THF, 1 mL, 1 mmol) solution and ethylenediamine (2 mL). The pH of the resulting solution was maintained at 9.8 and stirred overnight. The suspension that obtained was centrifuged and washed with water several times. Both samples were dried in an oven at 65–70 °C.

2.2. Characterization. Powder X-ray diffraction (PXRD) patterns of the samples were recorded using a Bruker diffractometer (D8 Discover) employing Cu K_α radiation (λ = 1.5418 Å) in the range of 2θ = 20–70°. The transmission electron microscopy (TEM) images and energy-dispersive X-ray (EDX) measurements were performed on the Philips Tecnai G^2 30 transmission electron microscope operating at an accelerating voltage of 300 kV. The scanning electron microscopy (SEM) images and EDX measurements were carried out using the FEI QUANTA 200 FEG scanning electron microscope. The mean size and size distribution of the samples were determined by dynamic light scattering experiments using DLS-ZP/Particle Sizer Nicomp 380 ZLS. Surface-area measurements were carried out using BELSORP mini II automatic specific surface area/pore size analyzer. Raman spectra of the samples in compact form were recorded using a Renishaw spectrophotometer equipped with microscope and Ar^+ laser (λ = 514.5 nm). Fourier transform (FT)-IR spectra of the samples were collected using Perkin-Elmer FT-IR spectrometer model 2000, employing KBr as dispersal medium. X-ray photoelectron spectroscopy (XPS) measurements were accomplished with a Thermo $K\alpha$ XPS instrument at a pressure of about 10^{-9} Torr. The core-level spectra of C 1s, O 1s, N 1s, F 1s, and Ce 3d were recorded using Mg $K\alpha$ radiation (photon energy = 1253.6 eV) at a pass energy of 50 eV, an electron take-off angle of 90°, and a resolution of 0.03 eV. The core-level spectra were fitted after adjusting the baseline relative to the signal background. The chemically distinct species were resolved using a Gaussian distribution fitting procedure with the peak positions, and areas were determined. The C 1s core-level spectra at 284.6 eV were taken as reference for the charge correction in the core-level spectra, and the peak positions were calibrated with respect to it. The elemental analysis of fluoride ions was quantified using a fluoride ion-selective electrode (Orion 96–09, Thermo Scientific) and an ion analyzer (Orion EA 940, Thermo Scientific). The magnetic measurements were carried out using a vibrating sample magnetometer (VSM) (Microsense EV9) at room temperature as well as using a superconducting quantum interference device (Ever Cool SQUID magnetometer) for variable-temperature magnetic susceptibility measurements (10–300 K). Diffuse reflectance spectra of the samples were collected on a Perkin-Elmer Lambda-35 UV–visible (UV–vis) spectrophotometer with an integrating sphere attached, using $BaSO_4$ as the reference. The photoluminescence (PL) measurements were performed using Horiba Jobin Yuvon Fluorolog-modular spectrofluorometer at room temperature, employing a continuous-wave (CW) xenon lamp source. NMR spectra were recorded using JEOL ECX-400P spectrometer, and mass spectra were recorded with a Waters KCL 455 Micromass using the electrospray ionization-mass spectrometry (ESI-MS) technique.

2.3. Photocatalytic Experiments. Photocatalytic studies were carried out using a 150 W mercury lamp along with a water filter to cut down IR radiation and glass cut-off filters to permit UV–vis radiation. Irradiation was carried out over an external Pyrex container with a volume of 250 mL, and water circulation was carried out to avoid any thermal effect. The catalyst (0.3 g) was added to 100 mL of an aqueous solution of methylene blue (MB) with an initial concentration of 15×10^{-6} mol/L in the Pyrex container with constant stirring to maintain a homogeneous suspension. Five milliliter aliquots were taken out periodically from the reaction mixture. The solutions were centrifuged, and the concentration of the solutions was determined by measuring the maximum absorbance (λ_{max} = 665 nm).

2.4. Catalytic Oxidative Coupling of Benzylamines to Imines—General Procedure. Benzylamine (1 mmol) and F-doped CeO_2/ CeO_2 (0.01 mmol) were taken in a Schlenk tube and fitted with O_2 balloon. The resulting heterogeneous mixture was heated at 110 °C, and the progress of the reaction was monitored by thin-layer chromatography (TLC). After the complete conversion of amine, the reaction mixture was cooled to room temperature and diluted with CH_2Cl_2 (5 mL). The catalyst was separated by filtration, and the filtrate was passed through the basic alumina-packed column using an ethylacetate and hexane (1:9) solvent mixture to obtain the N-(benzylidene)benzylamine product. The imine derivatives that were obtained by this procedure were characterized by NMR and mass spectral data.

3. RESULTS AND DISCUSSION

3.1. Structure, Morphology, and Composition Analysis by XPS. The PXRD patterns of the solids obtained from the preparations with and without the addition of tetrabutylammonium fluoride are presented in the Supporting Information, Figure S1. From the patterns, the fluorite structure of both products is quite evident, with the peak positions and intensities matching well with the JCPDS File No: 81−0792. The low-crystallite size of the product is also revealed by the broadness of the observed Bragg reflections. The structure refinement of the PXRD patterns of the samples were carried out by the Rietveld method using TOPAS 3 software in $Fm\bar{3}m$ space group[20] (Figure 1). Satisfactory Rietveld refinements of the PXRD patterns confirmed the fluorite structure (CeO_2) for both samples. The cubic lattice constant a, derived from the PXRD refinements of the samples obtained with and without
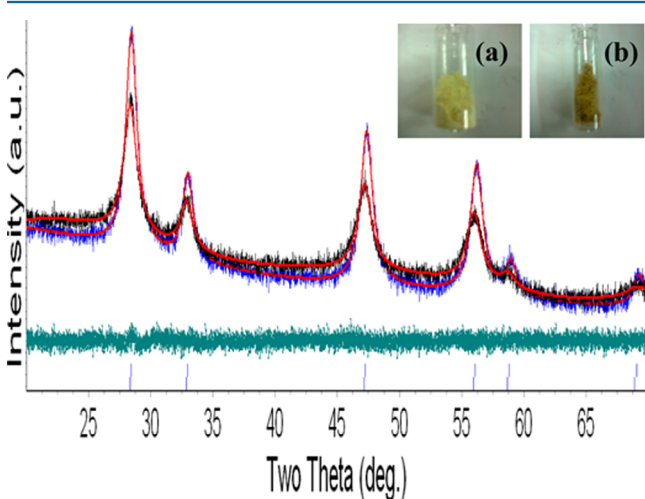

Figure 1. Final Rietveld fit of the observed PXRD patterns of sample prepared (blue) without and (black) with the use of fluorinating agent and residuum. Inset shows the digital photograph of the product (a) without and (b) with use of fluorinating agent.

the use of fluorinating agent, are 5.447 (3) Å and 5.428 (1) Å, respectively. The expansion of the unit cell clearly indicated the increased amount of Ce^{3+} in the CeO_2 samples obtained with the use of the fluorinating agent, as the radius of Ce^{3+} (8-coordinate; 1.14 Å) is higher than that of Ce^{4+} (8-coordinate; 0.97 Å).[21] From the Rietveld refinements (where crystallite size and strain comprised of Lorentzian and Gaussian component convolutions varying in 2θ as a function of $1/\cos(\theta)$ and $\tan(\theta)$, respectively[20]), the average crystallite sizes of the samples obtained with and without the use of the fluorinating agent were 7.9 and 10.6 nm, respectively. The yellow color typical of CeO_2 is noticed for the sample obtained without the use of the fluorinating agent, and light-brown colored powders resulted from the preparations carried out with the use of the fluorinating agent (inset of Figure 1).

A TEM image of the sample prepared with the addition of the fluorinating agent is shown in Figure 2a. Agglomeration of
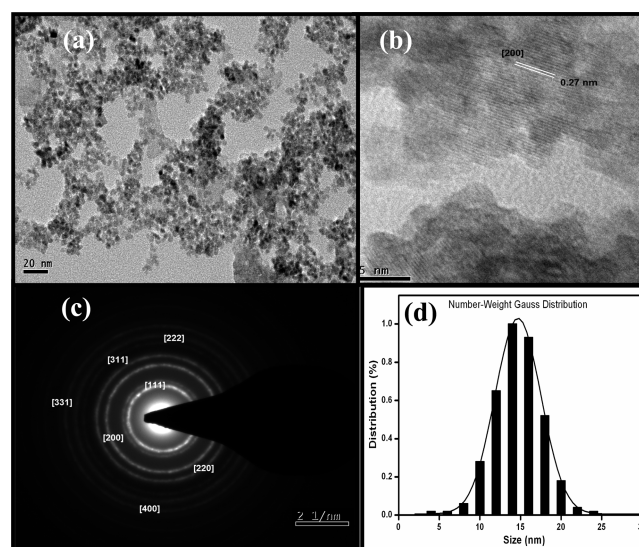

Figure 2. (a,b) TEM and HR-TEM images, respectively. (c) SAED pattern. (d) Histogram of the particle size of the sample obtained with the use of fluorinating agent from DLS experiments.

crystallites to a lesser extent was observed in the images. Lattice fringes of the individual crystallites, seen in the high-resolution (HR) TEM images, endorsed their high crystallinity (Figure 2b). The distances between the lattice fringes were 0.27 nm, corresponding to the d spacing of the (200) lattice plane of the cubic CeO_2 structure. The selected area electron diffraction (SAED) pattern of the crystallites (Figure 2c) could very well be indexed to the (111), (200), (220), (222), (311), (331), and (400) planes of the cubic fluorite structure. EDX spot analysis on various locations in TEM analysis confirmed uniform doping across the CeO_2 nanocrystals (see Supporting Information, Figure S2). The presence of fluoride in CeO_2 was also confirmed by SEM-EDX analysis (Supporting Information, Figure S3). A narrow distribution of nanocrystals having diameter in the 10−20 nm range, with an average value of 14.7 nm, has been calculated from the histogram of particle-size analysis (Figure 2d). This result is in good agreement with the size estimated from the TEM image and Rietveld refinement of the PXRD pattern. Diameters of majority of CeO_2 nanocrystals, from the particle-size measurement histogram, were in the 12−24 nm range, with an average value of about 18.3 nm (Supporting Information, Figure S4). The

surface area of F-doped CeO_2 and CeO_2, from the Brunauer-Emmett-Teller (BET) method, is 106.1 and 77.4 m²/g, respectively (Supporting Information, Figure S5). The experimentally reported density of CeO_2 is 7.28 g cm⁻³, and the density calculated from the Rietveld refinements for the compositions CeO_2 and $CeO_{1.68}F_{0.22}$ are 7.147 and 7.030 g cm⁻³, respectively.[22] The obvious contribution to the reduction in the density of CeO_2 and F-doped samples may be from the presence of oxygen vacancies. The higher reduction in density of F-doped sample can be due to the expansion of the crystal lattice, probably caused by the enhancement of Ce^{3+} concentration. Attempts to dope higher concentrations of fluoride (25 mol % and 40 mol %) have been unsuccessful, as reflections due to secondary CeF_3 phase appeared along with CeO_2 (Supporting Information, Figure S6). It is believed that the highly soluble cerium(III) nitrate undergoes oxidation to Ce(IV) at higher pH through hydroxide species formation, during which fluoride ion inclusion might have taken place.

Raman spectra of F-doped CeO_2 and CeO_2 are compared in Figure 3. The triply degenerate Raman active optical phonon
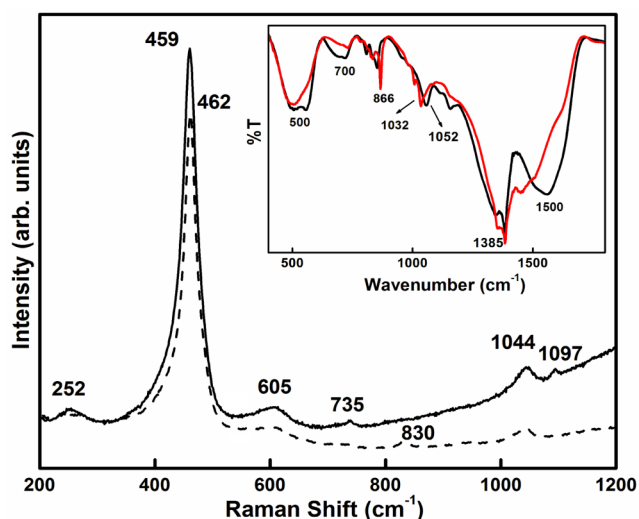
Figure 3. Raman spectra of (broken line) CeO_2 and (solid line) F-doped CeO_2 samples. Inset shows FT-IR spectra of (black) CeO_2 and (red) F-doped CeO_2.

(F_{2g}) mode is observed at 461 cm⁻¹ for CeO_2 and at 458 cm⁻¹ for the F-doped CeO_2.[23] This shift could possibly be due to the change in the cubic lattice constant.[23] Following earlier assignments, the band at around 461 cm⁻¹ was attributed to the interior phonon modes, and the bands at 252 and 420 cm⁻¹ were related to surface-related phonon modes.[24] Two weak second-order Raman bands at 605 and 830 cm⁻¹, related to the intrinsic oxygen vacancy defect modes (from the existence of $Ce^{3+}-V_O$ complex in the lattice), are observed for both F-doped CeO_2 and CeO_2 samples.[25] The extrinsic vacancy mode, mostly originating from different types of oxygen vacancy complexes formed upon doping, was present at 1097 cm⁻¹ in the F-doped CeO_2 sample. This may be the second-order Raman mode from a superoxide species (O_2^-).[26] The assignment of the bands at 735 and 1044 cm⁻¹ corresponds to the trace amounts of nitrate ions, as reported earlier.[27] The crystallite size of F-doped CeO_2 and CeO_2 samples has been estimated from the Raman line broadening using the following equation:[24]

$$\Gamma(\text{cm}^{-1}) = 10 + (124.7/d_g)(\text{nm}) \qquad (1)$$

where Γ (cm⁻¹) is the full-width at half-maximum of the Raman active mode peak and d_g is the crystallite size. The crystallite size of CeO_2 nanocrystals is 9.9 nm, and the crystallite size of the F-doped CeO_2 nanocrystals is 8.0 nm, which are in agreement with the particle size calculated from the TEM analysis as well as from the Rietveld refinements. The FT-IR spectra of F-doped CeO_2 and CeO_2 are presented in the inset of Figure 3. The O—O stretching band is observed at 1052 cm⁻¹ for CeO_2, and its position is shifted to 1032 cm⁻¹ on F-doping, indicating the introduction of highly electronegative anion.[28] In addition to the bands due to Ce—O vibrations, the appearance of a sharp band at 866 cm⁻¹, attributable to the Ce—F stretching, has confirmed the existence of direct Ce—F bonding in the doped sample.[26]

The valence/oxidation state of the elements and the surface composition of F-doped CeO_2 and CeO_2 have been analyzed by the XPS technique. In the N 1s spectrum, two low-intensity peaks located at 399 and 406 eV have been assigned to chemisorbed N_2 species and NO_3^- groups, respectively (see Supporting Information, Figure S7).[7a,29] The Ce 3d core-level X-ray photoelectron spectra consisting of peaks corresponding to Ce^{3+} and Ce^{4+} states have been fitted (Gaussian peak) following earlier reports (Figure 4a,b).[30] After fitting the Ce 3d core-level spectra, the percentage composition of Ce^{3+} and Ce^{4+} has been calculated using the relationships[31]

$$Ce^{3+} = v^0 + v' + u^0 + u' \qquad (2)$$

$$Ce^{4+} = v + v'' + v''' + u + u'' + u''' \qquad (3)$$

$$Ce^{3+} = Ce^{3+}/Ce^{3+} + Ce^{4+} \qquad (4)$$

where the bands labeled v collectively represent the Ce $3d_{5/2}$ ionization, and the ones labeled u represent the Ce $3d_{3/2}$ ionization. From the area under each peak, both of the samples have been found to be nonstoichiometric, with 70−78% of the Ce 3d photoemission due to Ce^{4+} and the remaining, that is, 30−22%, due to Ce^{3+}. Enhancement of the Ce^{3+} concentration (with the rest as Ce^{4+}) from 22% to 30% upon F-doping certainly justifies the charge compensation due to fluoride ion incorporation. The O 1s peak of F-doped CeO_2 and CeO_2 consists of four and three peaks, respectively (Figure 4c,d). The major component of the peak O^I in both of the samples, with binding energy of 529 eV, is attributed to the lattice oxygen of $Ce^{4+}-O^{2-}$, and the minor component O^{II}, with binding energy of 531 eV, is typical of the lattice oxygen of $Ce^{3+}-O^{2-}$.[32] The third peak component, at 532 eV in the doped sample, may be due to either defect-oxide or surface hydroxyl-like groups. As the Raman spectroscopy results indicated the presence of superoxide species, the assignment of the third peak to it is more meaningful. This fact is further supported from the work of Levasseur and co-workers,[33] who have assigned the peak in the 532−533 eV range to the ionized oxygen species that could allow compensation for some deficiencies in the subsurface of metal oxides. The formation of superoxide ions on the surface may be promoted by the presence of highly oxidizing fluorine available during the synthesis. A very low-intensity peak in the O 1s spectra at 542 eV observed in both samples may be due to some surface C—O species. The F 1s spectrum of the doped sample is nonsymmetric consisting of two peaks (inset of Figure 4d). While the peak located at 683.7 eV can be ascribed to physisorbed fluoride ions on the surface,[34] the peak located
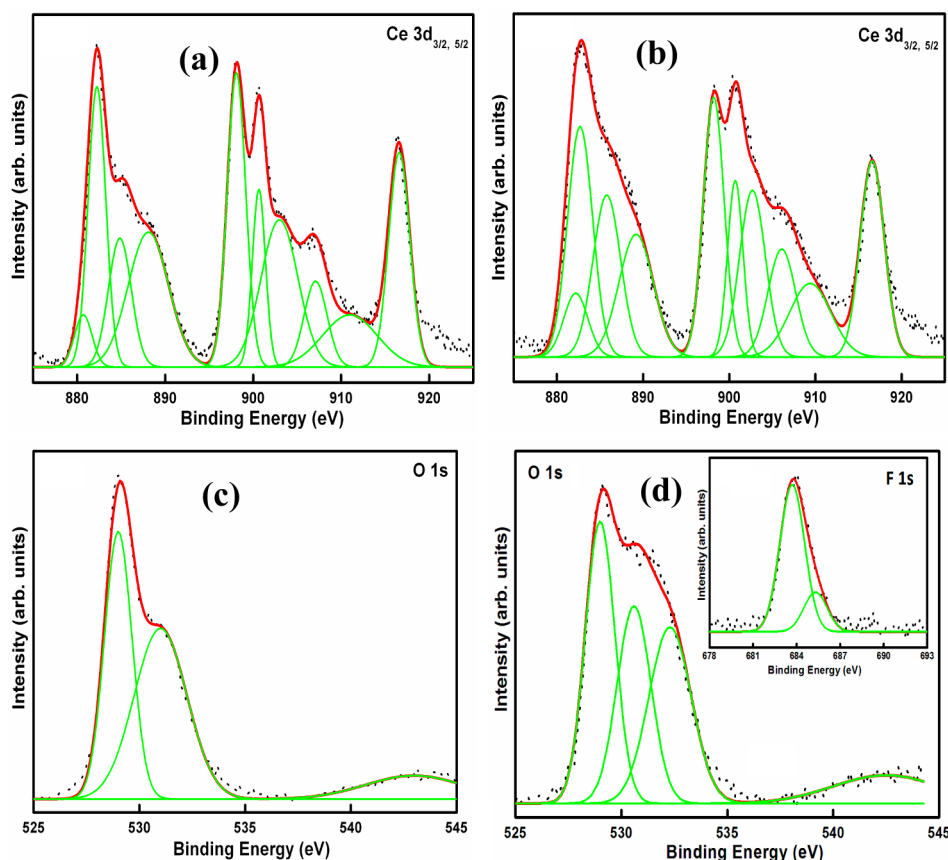
Figure 4. XPS core- level spectrum of (a,b) Ce 3d of CeO_2 and F-doped CeO_2. (c) O 1s of CeO_2. (d) O 1s and F 1s of F-doped CeO_2 nanocrystals.

at 685.4 eV has been attributed to chemically bound fluoride in the CeO_2 lattice.[35] This argument gathers additional support from the FT-IR spectroscopy results, where a band due to the vibration mode of Ce−F bond has been observed. The concentration of F^- ions has been calculated to be 10.8 atom %, which is very close to the nominal concentration of fluorinating agent used in the synthesis (10 %). The amount of fluoride ions in CeO_2 from chemical analysis was 8.1%, closer to the value observed with XPS analysis. As F^- and O^{2-} ions are of almost the same size, the doped fluoride ions may very well occupy the oxygen sites in the CeO_2 crystal lattice. A speculative pictorial representation of fluoride doping the CeO_2 lattice is presented in Figure 5, in which the Ce^{3+} ions, O_{vac}, and F^- ions are shown as blue, black, and green colored balls, respectively.

As fluoride-ion doping generated higher concentrations of Ce^{3+} (a paramagnetic species having a 4f unpaired electron with magnetic moment close to 2.54 μ_B), the magnetic susceptibility measurements of both pure and F-doped ceria have been

conducted in the temperature range of 10−300 K at an applied field of 1 T (Figure 6). The higher room-temperature molar susceptibility of F-doped sample (1.778×10^{-2} emu $mol^{-1}Oe^{1-}$) than the undoped sample (9.476×10^{-3} emu $mol^{-1}Oe^{1-}$) suggested the higher concentration of Ce^{3+} in the
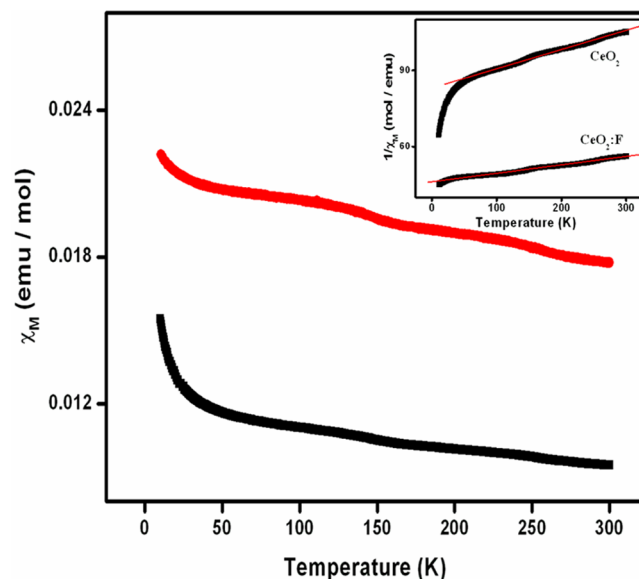

Figure 6. Magnetic susceptibility plots for (black) pure and (red) F-doped ceria samples at an applied field of 1 T in the temperature range of 10−300 K. Inset shows the thermal variation of inverse magnetic susceptibilities of CeO_2 and F-doped CeO_2.

Figure 5. Schematic diagram of CeO_2 with possible occupancies of the fluoride ions in the structure.

F-doped samples. While the magnetic susceptibility of CeF_3 follows a Curie–Weiss law versus the temperature (in the range between 100 and 300 K), CeO_2 has been assumed to be diamagnetic (with a susceptibility value of 0.6×10^{-4} emu/mol), and we subtracted its contribution. Quantification of Ce^{3+} in both samples was carried out by fitting the thermal variation of the inverse magnetic susceptibility (inset of Figure 6).[36] The results from the fitting procedure indicated the presence of 18.24% and 34.16% Ce^{3+} ion in the undoped sample and F-doped samples, respectively. These values are in conformity with the values estimated from XPS analysis. Nanosized (5–20 nm) ceria particles were reported to exhibit ferromagnetism at room temperature, possibly arising from the interaction of oxygen vacancies with the d and f orbitals of cerium near the Fermi level.[37] Presumably, such a scenario does not exist in these systems, as we observed only paramagnetic behavior in the magnetization versus magnetic field in the VSM measurements at room temperature (Supporting Information, Figure S8).

3.2. Optical Properties. CeO_2 is a wide band gap semiconductor (5.5 eV) whose Ce 4f and O 2p energy levels localize at the forbidden band and valence band at an energy gap of 3 eV. Generally, transitions at above 3 eV (Ce 4f→O 2p) are only observed for pure CeO_2, but the addition of dopants may create defect levels, which can lead to essentially absorption bands corresponding to band gap values around 3 eV.[38] In the UV–vis diffuse reflectance spectrum of CeO_2 and F-doped CeO_2, three major absorption bands at about 250, 280, and 330 nm have been observed. These have been assigned to charge transfer of O^{2-} to Ce^{3+}, O^{2-} to Ce^{4+}, and interband transitions, respectively (Figure 7).[39] Using the
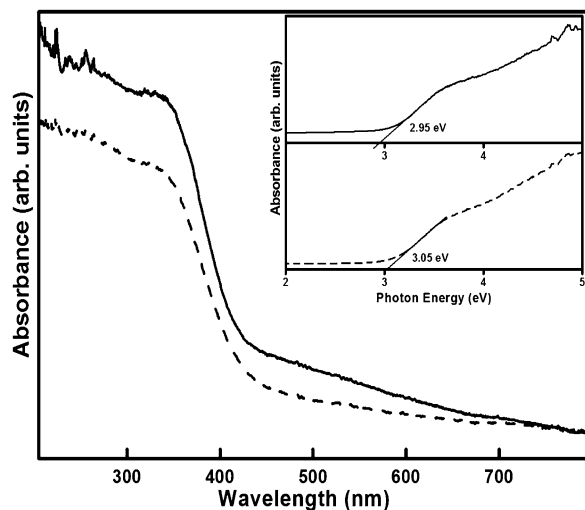

Figure 7. UV–visible diffuse reflectance spectra of (broken line) CeO_2 and (solid line) F-doped CeO_2 nanocrystals. Inset shows the bandgap estimation using the Kubelka–Munk function.

Kubelka–Munk function, the band gap of the CeO_2 was estimated to be 3.05 eV, which decreased to 2.95 eV on F^- doping (inset of Figure 7). The observed band gap narrowing of F-doped CeO_2 might be due to the change in electronic structure caused by the doping.[28] Demourgues and co-workers[5a] have described that the position and intensity of charge transfer (Ce 4f→O 2p) band observed in ceria is basically governed by the Ce–O chemical bonding influenced by the coordination number as well as the Ce–O bond

distances. The higher absorbance observed in F-doped CeO_2 over undoped CeO_2 can be explained based on the considerable increase in the ionic character of Ce–O chemical bonding due to the doping of high electronegative anion (F^-) for relatively less electronegative O^{2-} ions, as exemplified by Demourges and co-workers[5a] on (Ca^{2+}, F^-)-coupled substitution in CeO_2. These changes possibly tuned the charge-transfer band energy and thus imparted a higher UV-shielding property to the F-doped ceria.

F-doped and undoped CeO_2 have been evaluated as catalysts for the photo degradation of aqueous solution of MB dye under UV irradiation. The absorbance variations of MB solutions during the photo degradation and the adsorption of the catalyst in dark are shown in Figure 8 and Supporting Information,
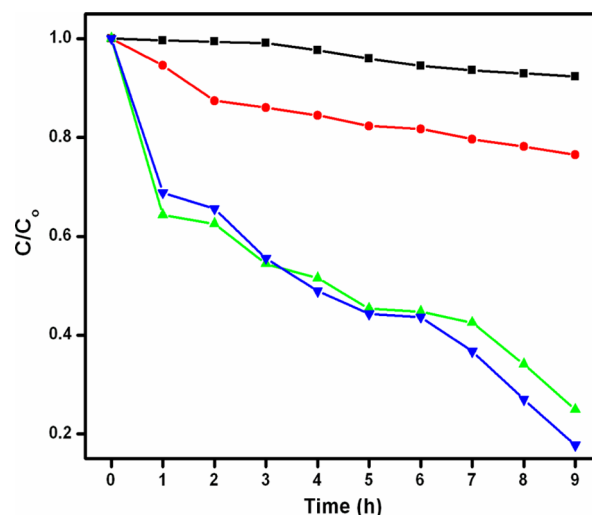

Figure 8. Photocatalytic degradation of MB dye over CeO_2 and F-doped CeO_2 nanocrystals. Square (■) and circle (●) represent the degradation using F-doped CeO_2 under dark and UV light, respectively, while triangle (▲) and inverted triangle (▼) represent the degradation using CeO_2 under dark and UV light, respectively.

Figure S9, respectively. The rates of degradation of MB solution in the absence and in the presence of UV light using F-doped CeO_2 nanocrystals are almost similar. In the absence of light irradiation, adsorption of MB dye is noticed on CeO_2 nanocrystals, and shining with UV radiation did not seem to bring any noticeable degradation of the dye solution. On the other hand, adsorption of dye solution over F-doped CeO_2 nanocrystals is found to be less, and the rate of photocatalytic degradation under UV irradiation was found to be negligible (Figure 8). Combining the photocatalytic inactivity with higher UV-shielding property of F-doped CeO_2 over CeO_2, it is proposed that the F-doped ceria will find potential use in cosmetic applications.

PL spectra of the CeO_2 and F-doped CeO_2 samples measured at λ_{ex} = 290 nm are shown in Figure 9. Two strong emission bands, observed at 322 and 341 nm, have been assigned to the parity-allowed transitions of the ^2D state to the spin–orbit components $^2F_{5/2}$ and $^2F_{7/2}$ of Ce^{3+}, respectively.[40] The energy difference between the two peaks is 19 nm, which is very close to calculated value of the ground state splitting of Ce^{3+}. The higher-emission intensities of the F-doped sample have confirmed the presence of higher concentration of Ce^{3+}. PL emission spectra of the F-doped CeO_2 sample at λ_{ex} = 420 nm (shown in Figure 9) consist of strong and broad emission
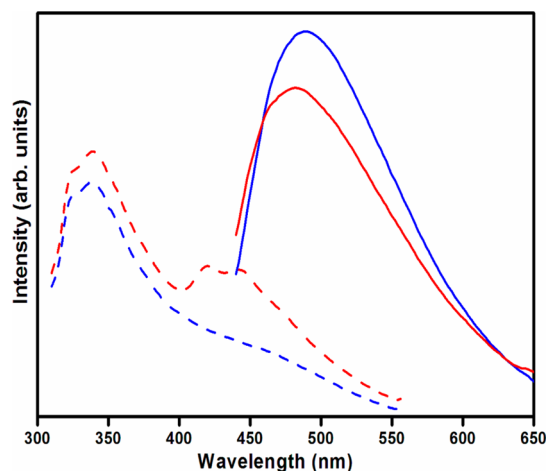
Figure 9. RTPL spectra of (blue line) CeO$_2$ and (red line) F-doped CeO$_2$ nanocrystals. Broken lines represent an excitation wavelength of 290 nm, while solid lines represent an excitation wavelength of 420 nm.

band at around 480 nm, arising primarily from the oxygen vacancies. A decrease in its intensity has indicated lower concentration of scattering centers and a high radiative recombination process. On close inspection, a small shift of the emission peak toward the shorter wavelength for the F-doped CeO$_2$ sample (as compared to the undoped CeO$_2$) has been noticed. In addition to these, two blue bands at 420 and 442 nm are observed for F-doped CeO$_2$ sample on exciting it with 290 nm radiation. All these transitions have indicated clearly the presence of oxygen vacancies in the doped sample.[41]

3.3. Application of CeO$_2$ and F-Doped CeO$_2$ as Catalysts for Oxidative Coupling of Benzylamines to Imines. First, the reaction of benzylamine (0.9 mmol) with F-doped CeO$_2$ (20 mol %) in organic solvents such as acetonitrile, 1, 2-dichloroethane, toluene, and p-xylene (1 mL) in the presence of aerial oxygen at refluxing temperature has been examined (Table 1). While no imine product is evident in acetonitrile and 1, 2-dichloroethane solvents (entries 1 and 2), and low yields of imine is observed in other reactions (entries 3 and 4). However, a notable amount of N-(benzylidene)benzylamine is formed after heating the amine and F-doped CeO$_2$ (20 mol %) suspension at 110 °C without any solvent (entry 5). Highest yield is obtained when the reaction is performed in the atmosphere of molecular oxygen,

using O$_2$ balloon (entry 6). The quantity of F-doped CeO$_2$ is decreased in the subsequent reactions and carried out in neat condition. When the catalyst loading is reduced to 10 mol %, the yield of imine is unchanged (entry 7). But with a further decrease of the catalyst loading to 5 mol %, an incomplete reaction is noticed even after extended time (entry 8). Therefore, a minimum of 10 mol % F-doped CeO$_2$ is required for a complete conversion of amine to imine in solvent-free condition.

Under the optimized conditions, a range of ortho-, meta-, and para-substituted benzylamines undergo coupling to their secondary imine dimers (Table 2). Electron-rich amines, such as p-methoxybenzylamine (87%, entry 2) and piperonylamine (79%, entry 3), and some electron-deficient amines, such as m,p-dichlorobenzylamine (81%, entry 5) and p-fluorobenzyl-amine (83%, entry 6), are readily converted to the secondary imines in high yields. More electron-deficient amine, namely, m,m-bis(trifluoromethyl)benzylamine (75%, entry 7) provided the corresponding imine in slightly lower yield. The methylenedioxy group of piperonylamine (entry 3) and halogen substituents (entries 4−7) are well-tolerated under the reaction conditions. Sterically bulky groups, such as o-chlorophenyl (75%, entry 4) and 1-naphthyl (72%, entry 8), cause only a slight diminution of yield. The heterocyclic amine such as 2-(amino methyl)thiophene (78%, entry 9) undergoes oxidative coupling, but furfurylamine (not shown) is not an efficient substrate.

We then investigated the oxidative coupling of benzylamines using CeO$_2$ (10 mol %) in the atmosphere of molecular oxygen under solvent-free conditions (Table 2). All the amine substrates that are oxidized with F-doped CeO$_2$ proceeded for the reaction of CeO$_2$, but the reactions are not completed even after prolonged duration (12 h); moreover, the reactions resulted in lower yield of imine products. The results summarized in Table 2 validate the superiority of F-doped CeO$_2$ over CeO$_2$. The higher catalytic efficiency of the fluoride-doped sample might be due to its lower particle size, higher Ce^{3+} concentration, and higher surface area as compared to undoped ceria.
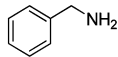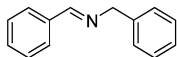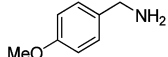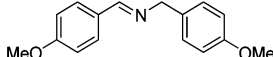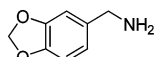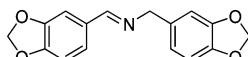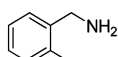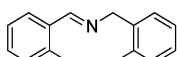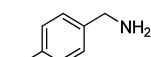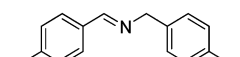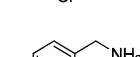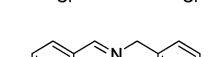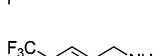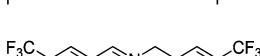
Finally, the recyclability of the F-doped CeO$_2$ catalyst was examined for oxidative coupling of benzylamine under standard reaction conditions. After the reaction was completed, the catalyst was recovered by filtration, washed with CH$_2$Cl$_2$, dried, and then used for the next reaction. We performed three recycling experiments, and the results are compiled in Table 3.

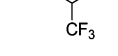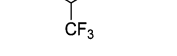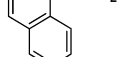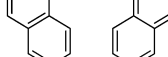**Table 1. Optimization of Reaction Conditions for F-Doped CeO$_2$ Catalyzed Oxidative Coupling of Benzylamine**[a]

entry	cat. (mol %)	solvent	temp. (°C)	time (h)	conv. (%)[b]
1	20	CH$_3$CN	82	12	
2	20	ClCH$_2$CH$_2$Cl	84	12	
3	20	toluene	111	12	9
4	20	p-xylene	138	12	17
5	20		110	12	58
6[c]	20		110	3	86
7[c]	10		110	3	86
8[c]	5		110	6	61

[a]Reactions carried out in aerobic conditions unless otherwise indicated. [b]Conversion determined by ^{1}H NMR analysis of the reaction mixture. [c]Reaction performed under the atmosphere of molecular oxygen.

Table 2. Oxidative Coupling of Various Benzylamines Using F-Doped CeO$_2$ and CeO$_2$ Catalysts[a]

Entry	Substrate	Product	Time (h)[b]	Isolated yield (%)[b,c]
1			3.0 (12)	86 (68)
2			5.0 (12)	87 (62)
3			5.5 (12)	79 (63)
4			5.0 (12)	75 (60)
5			4.5 (12)	81 (65)
6			4.5 (12)	83 (61)
7			5.5 (12)	75 (61)
8[d]			5.5 (12)	72 (60)
9[e]			6.5 (12)	78 (59)

[a]Reaction conditions: substrate (1 mmol), F-doped CeO$_2$ (0.01 mmol), 110 °C, and O$_2$ balloon. [b]The values in parentheses represent for the CeO$_2$-catalyzed reaction. [c]Isolated yield. [d]Formation of 18% 1-naphthaldehyde was observed by ^{1}H NMR analysis of the reaction mixture. [e]Toluene used as solvent.

Table 3. Recyclability of F-Doped CeO$_2$ Catalyst in the Oxidative Coupling of Benzylamine[a]

number of cycle	first cycle	second cycle	third cycle
isolated yield of imine (%)	86	81	76

[a]Reaction conditions: benzylamine (1 mmol) F-doped CeO$_2$ (0.01 mmol), 110 °C, 3h, O$_2$ balloon.

Yields of the imines after the recycling experiments declined marginally, which might possibly be due to a decrease in the concentration of active centers in the catalyst. However, the PXRD pattern of the catalyst after the third recycling experiment revealed that the structure is intact (see Supporting Information, Figure S10).

4. CONCLUSIONS

A nonhazardous solution-based method has been developed for the synthesis of fluoride-doped CeO$_2$ nanocrystals for the first time, using tetrabutylammonium fluoride as the fluorinating agent at room temperature. Doping in the lattice has been established by using various techniques. The fluoride doping has resulted in increased Ce^{3+} concentration in the samples, as revealed by PXRD, PL spectroscopy, XPS, and magnetic measurements. The band gap narrowed from 3.05 to 2.95 eV on F-doping in CeO$_2$. Higher UV-shielding capacity and photocatalytic inactivity of F-doped CeO$_2$ over CeO$_2$ for aqueous dye degradation suggested its potential for use in cosmetic applications. The higher Ce^{3+}/Ce^{4+} redox couple in the F-doped CeO$_2$ has successfully been utilized for the effective oxidative coupling of amines to imines under solvent-free conditions. The present catalytic systems have the following significant advantages from the standpoint of green chemistry: (i) the use of inexpensive and easily prepared catalysts, (ii) use of molecular oxygen as stoichiometric oxidant, (iii) no requirement for reaction solvent, (iv) applicability to various amine substrates, (v) heterogeneous catalysis, allowing facile catalyst/product separation, and (vi) reusability of the F-doped CeO$_2$ and CeO$_2$ catalysts. The F-doped CeO$_2$ served as a better catalyst and produced a high yield of imines in a short period, possibly due to its lower particle size and higher Ce^{3+} concentration as well as higher surface area than CeO$_2$.

■ ASSOCIATED CONTENT

Ⓢ Supporting Information

This includes PXRD patterns of products obtained with and without the use of fluorinating agent, TEM-EDX, SEM-EDX of

the CeO$_2$ sample obtained with the use of fluorinating agent, DLS histogram of CeO$_2$, BET surface area plots of CeO$_2$ and F-doped CeO$_2$ samples, PXRD patterns of the products obtained with the use of 25 and 40 mol % concentration of fluorinating agent, XPS core level of N 1s analysis of CeO$_2$ and F-doped CeO$_2$ samples, photo degradation of aqueous MB dye solution using CeO$_2$ and F-doped CeO$_2$, room-temperature M−H curves of CeO$_2$ and F-doped CeO$_2$ nanocrystals, PXRD pattern of the recycled catalysts, NMR spectra of imine products. This information is available free of charge via the Internet at http://pubs.acs.org.

■ AUTHOR INFORMATION

Corresponding Author

*E-mail: rnagarajan@chemistry.du.ac.in (R.N.), gopal@chemistry.du.ac.in (K.G.).

Notes

The authors declare no competing financial interest.

■ ACKNOWLEDGMENTS

■ REFERENCES

(1) (a) Murray, E. P.; Tsai, T.; Barnett, S. A. *Nature* **1999**, *400*, 649−651. (b) Corma, A.; Atienzar, P.; Garcia, H.; Chane-Ching, J.-Y. *Nature* **2004**, *3*, 394−397. (c) Izu, N.; Shin, W.; Murayama, N.; Kanzaki, S. *Sens. Actuators, B* **2002**, *87*, 95−98. (d) Park, S.; Vohs, J. M.; Gorte, R. J. *Nature* **2000**, *404*, 265−267.

(2) (a) Fu, Q.; Saltsburg, H.; Flytzani-Stephanopoulos, M. *Science* **2003**, *301*, 935−938. (b) Carrettin, S.; Concepcion, P.; Corma, A.; Nieto, J. M. L.; Puntes, V. F. *Angew. Chem., Int. Ed.* **2004**, *43*, 2538−2540.

(3) Singh, P.; Hegde, M. S. *J. Solid State Chem.* **2008**, *181*, 3248−3256.

(4) (a) Roy, S.; Hegde, M. S. *Catal. Commun.* **2008**, *9*, 811−815. (b) Gayen, A.; Priolkar, K. R.; Sarode, P. R.; Jayaram, V.; Hegde, M. S.; Subbanna, G. N.; Emura, S. *Chem. Mater.* **2004**, *16*, 2317−2328. (c) Sharma, S.; Hegde, M. S. *J. Chem. Phys.* **2009**, *130*, 114706 (1−8).

(5) (a) Sronek, L.; Majimel, J.; Kihn, Y.; Montardi, Y.; Tressaud, A.; Feist, M.; Legein, C.; Buzaré, J.-Y.; Body, M.; Demourgues, A. *Chem. Mater.* **2007**, *19*, 5110−5112. (b) Yabe, S.; Sato, T. *J. Solid State Chem.* **2003**, *171*, 7−11. (c) Lima, J. F.; de, R.; Martins, F.; Neri, C. R.; Serra, O. A. *Appl. Surf. Sci.* **2009**, *255*, 9006−9009. (d) Imanaka, N.; Masui, T.; Hirai, H.; Adachi, G.-Y. *Chem. Mater.* **2003**, *15*, 2289−2291. (e) Zholobak, N. M.; Ivanov, V. K.; Shcherbakov, A. B.; Shaporev, A. S.; Polezhaeva, O. S.; Baranchikov, A. Y.; Spivak, N. Y.; Tretyakov, Y. D. *J. Photochem. Photobiol., B* **2011**, *102*, 32−38.

(6) (a) Mogensen, M.; Lindegaard, T.; Hansen, U. R.; Mogensen, G. *J. Electrochem. Soc.* **1994**, *141*, 2122−2128. (b) Yahiro, H.; Eguchi, Y.; Eguchi, K.; Arai, H. *J. Appl. Electrochem.* **1988**, *18*, 527−531. (c) Wang, D. Y.; Park, D. S.; Griffith, J.; Nowick, A. S. *Solid State Ionics* **1981**, *2*, 95−105.

(7) (a) Jorge, A. B.; Fraxedas, J.; Cantarero, A.; Williams, A. J.; Rodgers, J.; Attfield, J. P.; Fuertes, A. *Chem. Mater.* **2008**, *20*, 1682−1684. (b) Mao, C.; Zhao, Y.; Qiu, X.; Zhu, J.; Burda, C. *Phys. Chem. Chem. Phys.* **2008**, *10*, 5633−5638. (c) Sun, D.; Gu, M.; Li, R.; Yin, S.; Song, X.; Zhao, B.; Li, C..; Li, J.; Feng, Z.; Sato, T. *Appl. Surf. Sci.* **2013**, *280*, 693−697. (d) Jorge, A. B.; Sakatani, Y.; Boissière, C.; Laberty-Roberts, C.; Sauthier, G.; Fraxedas, J.; Sanchez, C.; Fuertes, A. *J. Mater. Chem.* **2012**, *22*, 3220−3226.

(8) Jorda, J. L.; Adorian, J.; Desre, D. P. *J. Less-Common Met.* **1990**, *157*, 327−334.

(9) (a) Miedziak, P. J.; Tang, Z.; Davies, T. E.; Enache, D. I.; Bartley, J. K.; Carley, A. F.; Herzing, A. A.; Kiely, C. J.; Taylor, S. H.; Hutchings, G. J. *J. Mater. Chem.* **2009**, *19*, 8619−8627. (b) Sutradhar, N.; Sinhamahapatra, A.; Pahari, S.; Jayachandran, M.; Subramanian, B.; Bajaj, H. C.; Panda, A. B. *J. Phys. Chem. C* **2011**, *115*, 7628−7637. (c) Júarez, R.; Corma, A.; Garćıa, H. *Green Chem.* **2009**, *11*, 949−952. (d) Sun, Z.; Zhang, H.; An, G.; Yang, G.; Liu, Z. *J. Mater. Chem.* **2010**, *20*, 1947−1952.

(10) Adams, J. P. *J. Chem. Soc., Perkin Trans. 1* **2000**, 125−139.

(11) (a) Bloch, R. *Chem. Rev.* **1998**, *98*, 1407−1438. (b) Kobayashi, S.; Ishitani, H. *Chem. Rev.* **1999**, *99*, 1069−1094. (c) Pàmies, O.; Éll, A. H.; Samec, J. S. M.; Hermanns, N.; Bäckvall, J.-E. *Tetrahedron Lett.* **2002**, *43*, 4699−4702. (d) Hermanns, N.; Dahmen, S.; Bolm, C.; Bräse, S. *Angew. Chem., Int. Ed.* **2002**, *41*, 3692−3694. (e) Török, B.; Surya Prakash, G. K. *Adv. Synth. Catal.* **2003**, *345*, 165−168.

(12) (a) Hu, Z.; Kerton, F. M. *Org. Biomol. Chem.* **2012**, *10*, 1618−1624. (b) Largeron, M.; Fleury, M.-B. *Angew. Chem., Int. Ed.* **2012**, *51*, 5409−5412. (c) Patil, R. D.; Adimurthy, S. *RSC Adv.* **2012**, *2*, 5119−5122. (d) Patil, R. D.; Adimurthy, S. *Adv. Synth. Catal.* **2011**, *353*, 1695−1700.

(13) (a) So, M.-H.; Liu, Y.; Ho, C.-M.; Che, C.-M. *Chem.—Asian J.* **2009**, *4*, 1551−1561. (b) Grirrane, A.; Corma, A.; Garcia, H. *J. Catal.* **2009**, *264*, 138−144. (c) Aschwanden, L.; Mallat, T.; Krumeich, F.; Baiker, A. *J. Mol. Catal. A: Chem.* **2009**, *309*, 57−62. (d) Aschwanden, L.; Panella, B.; Rossbach, P.; Keller, B.; Baiker, A. *ChemCatChem* **2009**, *1*, 111−115. (e) Zhu, B.; Lazar, M.; Trewyn, B. G.; Angelici, R. J. *J. Catal.* **2008**, *260*, 1−6. (f) Zhu, B.; Angelici, R. J. *Chem. Commun.* **2007**, 2157−2159.

(14) Zhang, E.; Tian, H.; Xu, S.; Yu, X.; Xu, Q. *Org. Lett.* **2013**, *15*, 2704−2704.

(15) He, W.; Wang, L.; Sun, C.; Wu, K.; He, S.; Chen, J.; Wu, P.; Yu, Z. *Chem.—Eur. J.* **2011**, *17*, 13308−13317.

(16) (a) Kodama, S.; Yoshida, J.; Nomoto, A.; Ueta, Y.; Yano, S.; Ueshima, M.; Ogawa, A. *Tetrahedron Lett.* **2010**, *51*, 2450−2452. (b) Nakayama, K.; Hamamoto, M.; Nishiyama, Y.; Ishii, Y. *Chem. Lett.* **1993**, *22*, 1699−1702. (c) Neumann, R.; Levin, M. *J. Org. Chem.* **1991**, *56*, 5707−5710.

(17) (a) Lang, X.; Ma, W.; Zhao, Y.; Chen, C.; Ji, H.; Zhao, J. *Chem.—Eur. J.* **2012**, *18*, 2624−2631. (b) Lang, X.; Ji, H.; Chen, C.; Ma, W.; Zhao, J. *Angew. Chem., Int. Ed.* **2011**, *50*, 3934−3937.

(18) Furukawa, S.; Ohno, Y.; Shishido, T.; Teramura, K.; Tanaka, T. *ACS Catal.* **2011**, *1*, 1150−1153.

(19) Al-Hmoud, L.; Jones, C. W. *J. Catal.* **2013**, *301*, 116−124.

(20) (a) Rietvield, H. M. *J. Appl. Crystallogr.* **1969**, *2*, 65−71. (b) Coelho, A. A. *TOPAS, version 3.1*; Bruker AXS GmbH: Karlsruhe, Germany, 2003. (c) Balzar, D. Voigt-Function Model in Diffraction Line-Broadening Analysis, in Defect and Microstructure Analysis from Diffraction. In *International Union of Crystallography Monographs on Crystallography No. 10*; Snyder, R.L., Bunge, H.J., Fiala, J. Eds.; Oxford University Press: New York, 1999.

(21) Shannon, R. D.; Prewitt, C. T. *Acta Crystallogr. B.* **1969**, *25*, 925−946.

(22) Ho, C.; Yu, J. C.; Kwong, T.; Mak, A. C.; Lai, S. *Chem. Mater.* **2005**, *17*, 4514−4522.

(23) Spanier, J. E.; Robinson, R. D.; Zhang, F.; Chan, S.-W.; Herman, I. P. *Phys. Rev. B* **2001**, *64*, 245407 (1−8).

(24) Weber, W. H.; Bass, K. C.; McBride, J. R. *Phys. Rev. B* **1993**, *48*, 178−185.

(25) Guo, M.; Lu, J.; Wu, Y.; Wang, Y.; Luo, M. *Langmuir* **2011**, *27*, 3872−3877.

(26) Nakamoto, K. *Infrared and Raman Spectra of Inorganic and Coordination Compounds*; John Wiley & Sons, Inc.: Hoboken, NJ, 2009.

(27) Palard, M.; Balencie, J.; Maguer, A.; Hochepied, J.-F. *Mater. Chem. Phys.* **2010**, *120*, 79−88.

(28) Ahmad, S.; Kharkwal, M.; Govind; Nagarajan, R. *J. Phys. Chem. C* **2011**, *115*, 10131−10139.

(29) Kasten, L. S.; Grant, J. T.; Grebasch, N.; Voevodin, N.; Arnold, F. E.; Donley, M. S. *Surf. Coat. Technol.* **2001**, *140*, 11−15.

(30) (a) Burroughs, P.; Hamnett, A.; Orchard, A. F.; Thornton, G. *Dalton Trans.* **1976**, 1686−1692. (b) Romeo, M.; Bak, K.; Fallah, J. E.; Normand, F. L.; Hilaire, L. *Surf. Interface Anal.* **1993**, *20*, 508−512. (c) Pfau, A.; Schierbaum, K. D. *Surf. Sci.* **1994**, *321*, 71−80.

(31) Preisler, E. J.; Marsh, O. J.; Beach, R. A.; McGill, T. C. *J. Vac. Sci. Technol., B: Microelectron. Nanometer Struct.—Process., Meas., Phenom.* **2001**, *19*, 1611−1618.

(32) (a) Fang, J.; Bi, X.; Si, D.; Jiang, Z.; Huang, W. *Appl. Surf. Sci.* **2007**, *253*, 8952−8961. (b) Santra, C.; Rahman, S.; Bojja, S.; James, O. O.; Sen, D.; Maity, S.; Mohanty, A. K.; Mazumder, S.; Chowdhury, B. *Catal. Sci. Technol.* **2013**, *3*, 360−370.

(33) Dupin, J.-C.; Gonbeau, D.; Vinatier, P.; Levasseur, A. *Phys. Chem. Chem. Phys.* **2000**, *2*, 1319−1324.

(34) Li, D.; Ohashi, N.; Hishita, S.; Kolodiazhnyi, T.; Haneda, H. *J. Solid State Chem.* **2005**, *178*, 3293−3302.

(35) (a) Todorova, N.; Giannakopoulou, T.; Romanos, G.; Vaimakis, T.; Yu, J.; Trapalis, C. *Int. J. Photoenergy* **2008**, 534038 (1−8). (b) Yu, J. C.; Yu, J.; Ho, W.; Jiang, Z.; Zhang, L. *Chem. Mater.* **2002**, *14*, 3808−3816. (c) Zhou, J. K.; Lv, L.; Yu, J.; Li, H. L.; Guo, P.-Z.; Sun, H.; Zhao, X. S. *J. Phys. Chem. C* **2008**, *112*, 5316−5321.

(36) (a) Laachir, A.; Perrichon, V.; Badri, A.; Lamotte, J.; Catherine, E.; Lavalley, J. C.; Fallah, J. E.; Hilaire, L.; Normand, F.; Quemere, E.; Sauvion, G. N.; Touret, O. *J. Chem. Soc., Faraday Trans.* **1991**, *87*, 1601−1609. (b) Chan, G. H.; Deng, B.; Bertoni, M.; Ireland, J. R.; Hersam, M. C.; Mason, T. O.; Duyne, R. P. V.; Ibers, J. A. *Inorg. Chem.* **2006**, *45*, 8264−4272.

(37) (a) Shah, L. R.; Ali, B.; Zhu, H.; Wang, W. G.; Song, Y. Q.; Zhang, H. W.; Shah, S. I.; Xiao, J. Q. *J. Phys.: Condens. Matter* **2009**, *21*, 486004 (1−9). (b) Sundaresan, A.; Bhargavi, R.; Rangarajan, N.; Siddesh, U.; Rao, C. N. R. *Phys. Rev. B* **2006**, *74*, 161306 (1−4).

(38) (a) Sun, C.; Li, H.; Zhang, H.; Wang, Z.; Chen, L. *Nanotechnology* **2005**, *16*, 1454−1463. (b) Boring, A. M.; Wood, J. H. *Solid State Commun.* **1983**, *47*, 227−232. (c) Marabelli, F.; Wachter, P. *Phys. Rev. B* **1987**, *36*, 1238−1243.

(39) (a) Rao, G. R.; Sahu, H. R. *Proc.—Indian Acad. Sci., Chem. Sci.* **2001**, *113*, 651−658. (b) Bensalem, A.; Muller, J. C.; Bozon-Verduraz, F. *J. Chem. Soc., Faraday Trans.* **1992**, *88*, 153−154.

(40) (a) Yu, M.; Lin, J.; Fu, J.; Zhang, H. J.; Han, Y. C. *J. Mater. Chem.* **2003**, *13*, 1413−1419. (b) Wang, Z. L.; Quan, Z. W.; Jia, P. Y; Lin, C. K.; Luo, Y.; Chen, Y.; Fang, J.; Zhou, W.; O'Connor, C. J.; Lin, J. *Chem. Mater.* **2006**, *18*, 2030−2037.

(41) Wang, Z.; Quan, Z.; Lin, J. *Inorg. Chem.* **2007**, *46*, 5237−5242.